Time-resolved investigation of nanometer scale deformations induced by a high flux x-ray beam

J. Gaudin,[1,*] B. Keitel,[2] A. Jurgilaitis,[3] R. Nüske,[3] L. Guérin,[4] J. Larsson,[3] K. Mann,[5] B. Schäfer,[5] K. Tiedtke,[2] A. Trapp,[1] Th. Tschentscher,[1] F. Yang,[1] M. Wulff,[4] H. Sinn,[1] and B. Flöter[5]

[1]*European XFEL, Albert-Einstein-Ring 19, D-22761 Hamburg, Germany*
[2]*Deutsches Elektronen-Synchrotron, Notkestraße 85, D-22603 Hamburg, Germany*
[3]*Department of Physics, Lund University, P.O. Box 118, 221 00 Lund, Sweden*
[4]*European Synchrotron Radiation Facility, 6 rue Jules Horowitz, 38043 Grenoble, France*
[5]*Laser-Laboratorium Göttingen, Hans-Adolf-Krebs-Weg 1, D-37077 Göttingen, Germany*
*jerome.gaudin@xfel.eu

Abstract: We present results of a time-resolved pump-probe experiment where a Si sample was exposed to an intense 15 keV beam and its surface monitored by measuring the wavefront deformation of a reflected optical laser probe beam. By reconstructing and back propagating the wavefront, the deformed surface can be retrieved for each time step. The dynamics of the heat bump, build-up and relaxation, is followed with a spatial resolution in the nanometer range. The results are interpreted taking into account results of finite element method simulations. Due to its robustness and simplicity this method should find further developments at new x-ray light sources (FEL) or be used to gain understanding on thermo-dynamical behavior of highly excited materials.

©2011 Optical Society of America

OCIS codes: (340.0340) X-ray optics; (160.4670) Optical materials; (140.2600) Free-electron lasers (FELs).

References and links

1. S. Qian, W. Jark, G. Sostero, A. Gambitta, F. Mazzolini, and A. Savoia, "Precise measuring method for detecting the in situ distortion profile of a high-heat-load mirror for synchrotron radiation by use of a pentaprism long trace profiler," Appl. Opt. **36**(16), 3769–3775 (1997).
2. J. Susini, R. Baker, M. Krumrey, W. Schwegle, and I. Kvick, "Adaptive x-ray mirror prototype: first results," Rev. Sci. Instrum. **66**(2), 2048–2052 (1995).
3. P. Revesz and A. Kazimirov, "In situ measurements of thermal distortions in synchrotron optics under high heat load," Synchrotron Radiation News **23**(1), 32–35 (2010).
4. W. Ackermann, G. Asova, V. Ayvazyan, A. Azima, N. Baboi, J. Bähr, V. Balandin, B. Beutner, A. Brandt, A. Bolzmann, R. Brinkmann, O. I. Brovko, M. Castellano, P. Castro, L. Catani, E. Chiadroni, S. Choroba, A. Cianchi, T. Costello, D. Cubaynes, J. Dardis, W. Decking, H. Delsim-Hashemi, A. Delserieys, G. Di Pirro, M. Dohlus, S. Düsterer, A. Eckhardt, T. Edwards, B. Faatz, J. Feldhaus, K. Flöttmann, J. Frisch, L. Fröhlich, T. Garvey, U. Gensch, Ch. Gerth, M. Görler, N. Golubeva, H.-J. Grabosch, M. Grecki, O. Grimm, K. Hacker, U. Hahn, J. H. Han, K. Honkavaara, T. Hott, M. Hüning, Y. Ivanisenko, E. Jaeschke, W. Jalmuzna, T. Jezynski, R. Kammering, V. Katalev, K. Kavanagh, E. T. Kennedy, S. Khodyachykh, K. Klose, V. Kocharyan, M. Körfer, M. Kollewe, W. Koprek, S. Korepanov, D. Kostin, M. Krassilnikov, G. Kube, M. Kuhlmann, C. L. S. Lewis, L. Lilje, T. Limberg, D. Lipka, F. Löhl, H. Luna, M. Luong, M. Martins, M. Meyer, P. Michelato, V. Miltchev, W. D. Möller, L. Monaco, W. F. O. Müller, O. Napieralski, O. Napoly, P. Nicolosi, D. Nölle, T. Nuñez, A. Oppelt, C. Pagani, R. Paparella, N. Pchalek, J. Pedregosa-Gutierrez, B. Petersen, B. Petrosyan, G. Petrosyan, L. Petrosyan, J. Pflüger, E. Plönjes, L. Poletto, K. Pozniak, E. Prat, D. Proch, P. Pucyk, P. Radcliffe, H. Redlin, K. Rehlich, M. Richter, M. Roehrs, J. Roensch, R. Romaniuk, M. Ross, J. Rossbach, V. Rybnikov, M. Sachwitz, E. L. Saldin, W. Sandner, H. Schlarb, B. Schmidt, M. Schmitz, P. Schmüser, R. Schneider, A. Schneidmiller, S. Schnepp, S. Schreiber, M. Seidel, D. Sertore, V. Shabunov, C. Simon, S. Simrock, E. Sombrowski, A. Sorokin, P. Spanknebel, R. Spesyvtsev, L. Staykov, B. Steffen, F. Stephan, F. Stulle, H. Thom, K. Tiedtke, M. Tischer, S. Toleikis, R. Treusch, D. Trines, I. Tsakov, E. Vogel, T. Weiland, H. Weise, M. Wellhöfer, M. Wendt, I. Will, A. Winter, K. Wittenburg, W. Wurth, P. Yeates, V. Yurkov, I. Zagorodnov, and K. Zapfe, "Operation of a free-electron laser from the extreme ultraviolet to the water window," Nat. Photonics **1**(6), 336–342 (2007).
5. P. Emma, R. Akre, J. Arthur, R. Bionta, C. Bostedt, J. Bozek, A. Brachmann, P. Bucksbaum, R. Coffee, F.-J. Decker, Y. Ding, D. Dowell, S. Edstrom, A. Fisher, J. Frisch, S. Gilevich, J. Hastings, G. Hays, Ph. Hering, Z. Huang, R. Iverson, H. Loos, M. Messerschmidt, A. Miahnahri, S. Moeller, H.-D. Nuhn, G. Pile, D. Ratner, J. Rzepiela, D. Schultz, T. Smith, P. Stefan, H. Tompkins, J. Turner, J. Welch, W. White, J. Wu, G. Yocky, and J.

Galayda, "First lasing and operation of an angstrom-wavelength free-electron laser," Nat. Photonics **4**(9), 641–647 (2010).

6. A. Barty, R. Soufli, T. McCarville, S. L. Baker, M. J. Pivovaroff, P. Stefan, and R. Bionta, "Predicting the coherent x-ray wavefront focal properties at the Linac Coherent Light Source (LCLS) x-ray free electron laser," Opt. Express **17**(18), 15508–15519 (2009).
7. G. Geloni, E. Saldin, L. Samoylova, E. Schneidmiller, H. Sinn, Th. Tschentscher, and M. Yurkov, "Coherence properties of the European XFEL," N. J. Phys. **12**(3), 035021 (2010).
8. F. Siewert, J. Buchheim, and T. Zeschke, "Characterization and calibration of 2nd generation slope measuring profiler," Nucl. Instrum. Meth. Phys. Res. Sect. A Accelerators, Spectrometers, Detectors Assoc. Equipment **616**(2-3), 119–127 (2010).
9. A. R. B. de Castro, A. R. Vasconcellos, and R. Luzzi, "Thermoelastic analysis of a silicon surface under x-ray free-electron-laser irradiation," Rev. Sci. Instrum. **81**(7), 073102 (2010).
10. A. R. B. de Castro, A. R. Vasconcellos, and R. Luzzi, " "Erratum: 'Thermoelastic analysis of a silicon surface under x-ray free-electron-laser irradiation'," Rev. Sci. Instrum. **82**(4), 049901 (2011).
11. B. Schäfer, J. Gloger, U. Leinhos, and K. Mann, "Photo-thermal measurement of absorptance losses, temperature induced wavefront deformation and compaction in DUV-optics," Opt. Express **17**(25), 23025–23036 (2009).
12. J. Hartmann, "Bemerkungen über den Bau und die Justirung von Spektrographen," Z. Instrumentenkd **1900**(20), 47 (1900).
13. J. Hoszowska, J.-S. Migliore, V. Mocella, C. Ferrero, A. K. Freund, and L. Zhang, "Performance of synchrotron x-ray monochromators under heat load Part 1: finite element modeling," Nucl. Instrum. Meth. Phys. Res. Sect. A Accelerators, Spectrometers, Detectors Assoc. Equipment **467-468**, 409–413 (2001).
14. T. K. Kim, J. H. Lee, M. Wulff, Q. Kong, and H. Ihee, "Spatiotemporal kinetics in solution studied by time-resolved X-ray liquidography (solution scattering)," ChemPhysChem **10**(12), 1958–1980 (2009).
15. M. Born and E. Wolf, *Principles of Optics,* 6th ed. (Cambridge University Press, Cambridge, 1985)
16. D. R. Neal, W. J. Alford, J. K. Gruetzner, and M. E. Warren, "Amplitude and phase beam characterization using a two-dimensional wavefront sensor," Proc. SPIE **2870**, 72–82 (1996).
17. B. Schäfer and K. Mann, "Investigation of the propagation characteristics of excimer lasers using a Hartmann-Shack sensor," Rev. Sci. Instrum. **71**(7), 2663–2668 (2000).
18. J. J. Wortman and R. A. Evans, "Young's modulus, shear modulus, and Poisson's ratio in silicon and germanium," J. Appl. Phys. **36**(1), 153–156 (1965).

1. Introduction

The dynamics of a surface submitted to high heat load or to high excitation is of great interest from both fundamental and application points of view. From the application point of view, it has been addressed in the case of synchrotron optics (mirrors as well as crystal monochromators) where measurements have been performed using different techniques like in situ long trace profilers [1], or different types of Hartmann-Shack sensors [2,3]. These measurements provided sub-micron resolution in terms of height deformation, but only under steady state load. In the case of 4th generation x-ray light sources linear accelerator based lasers, so called Free Electron Lasers (FELs) [4,5] which deliver ultra-short coherent light pulses, deformations of optics are even less tolerable. In fact the intrinsic properties of FEL beams put high constraints on the optics/beamline design. A key parameter is the wavefront, firstly since it determines the focusing properties of the beam [6], and secondly because a highly distorted wavefront leads to effects similar to coherence loss [7]. While the manufacturing related static surface figure can be controlled with extremely high precision using slope measuring deflectometry techniques [8], the in situ performance of FEL optics will also strongly depend on the performance under heat load. It has been shown that for 0.1 nm radiation the surface flatness should be better than 2 nm over a 800 mm long grazing incidence optics [7]. From a more fundamental point of view, models have been developed [9,10] to describe the specific case of a single FEL pulse, providing insight on the kinetics of the deformation. However, no results of time-resolved measurements were published so far. In this article, we report on such kind of time-resolved investigations in the case of a bunch train of x-ray pulses at MHz repetition rate.

The experiment was performed at the ID09 beamline at the European Synchrotron Radiation Facility (ESRF). This beamline accomplishes both high x-ray flux and a dedicated setup for time-resolved studies. The wavefront of a reflected femtosecond optical laser was measured at different time steps after having exposed the sample to a high flux x-ray pulse train. Specific wavefront retrieval and back propagation allowed reconstruction of the heat bump induced on the surface of an optical element. The measurement was performed using a highly sensitive Hartmann-Shack sensor, which had already been employed to monitor

wavefront distortions due to thermal lensing in fused silica with sub-nm accuracy [11]. Due to their high relative sensitivity with respect to a known reference wavefront and robustness, Hartmann-type measurements are well suited for photothermal measurements. Actually, the measurement of thermal distortions in a collimating objective was one of the very first applications Hartmann presented in his landmark paper on the new wavefront sensing technique in 1900 [12]. Finally we used the Finite Element Method (FEM) to model the experiments. This method is routinely used to predict behavior of x-ray optics under static heat load [13]. In this specific experiment the dynamics behavior has also been modeled.

After a presentation of the experimental setup and the measurement method (sect. 2) the procedure to retrieve the bump height from the measured wavefront is described (sect. 3). Detailed FEM simulations are described (sect. 4) and results are compared and discussed in the last section (sect. 5).

2. Experimental setup and procedure

2.1 Description of the setup

The experiment was performed at the ID09B beamline at the ESRF. This beamline provides quasi-monochromatic ("pink beam") intense x-ray pulses (pulse width 100 ps) synchronized with a near infra-red (NIR) femtosecond laser ($\lambda = 780$ nm), delivering 2 mJ / pulse within 100 fs. The setup allows performing pump-probe experiments where usually the optical laser represents the pump and x-ray pulses act as probe [14]. In our specific case a 82 µs long bunch train of 120 x-ray pulses selected by a high speed shutter was used as pump and a single NIR pulse as probe, both running at one kilohertz repetition rate. The experimental setup is displayed in Fig. 1.
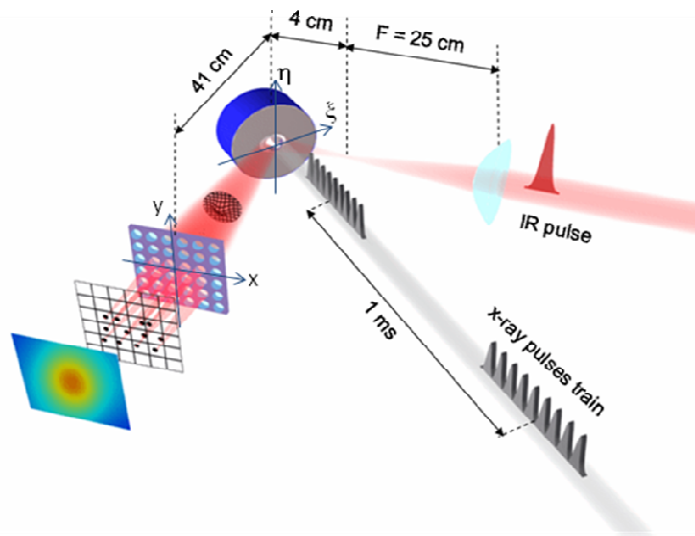

Fig. 1. Schematic view of the experimental setup

The undulators were tuned to deliver the peak intensity at 15 keV in the 4 bunch mode, i.e. the mode providing the highest photon flux. The estimated energy per pulse from a calibrated photodiode was 2.7 µJ. The 82 µs bunch train was focused at normal incidence onto the target within a spot of 125 µm x 64 µm (full width half maximum, as measured by a knife-edge scan) in order to maximize the photon flux on the sample. In order to improve its wavefront, the NIR laser beam was spatially filtered using an in-vacuum pinhole and attenuated to 5 nJ/pulse before reaching the sample. A spherical lens (focal length f = 25 cm) focused the laser under an incidence angle of 41° onto the sample positioned in the divergent beam 4 cm behind the focal plane. The reflected NIR radiation was monitored by a Hartmann-Shack wavefront sensor located at a distance of 41 cm from the sample. The Hartmann-Shack sensor

developed by Laser-Laboratorium Göttingen consists of a digital CCD camera (12 bit, 1280 x 1024 pixels, 6.45 µm pixel size) placed behind an array of plano-convex quartz micro-lenses (f = 40 mm, pitch 0.3 mm). The camera was synchronized with the NIR pulse. The overall setup was covered to avoid perturbations of the probe laser beam due to air flow. The experimental geometry introduced here, using a divergent test laser beam, enables the measurement of wavefront distortions which are laterally smaller than the microlens array pitch. The sample surface topology is computed using numerical Fresnel propagation methods.

We choose to study Si as it is commonly used as x-ray mirror substrate and x-ray crystal monochromator. The sample consists of a super smooth Si substrate (flatness λ/10 @ 633 nm, rms roughness 1 Å). Silicon was coated with a 100 nm thick layer of Platinum. At normal incidence the Platinum coating absorbs only 3% of the incoming radiation, hence being almost transparent for the x-rays. However, the metallic coating acts as a perfect mirror for the NIR laser, avoiding heating of the sample by the test laser beam.

2.2 Measurement procedure

Before performing the experiment, both spatial and temporal overlap of the pump and probe beams had to be accomplished. Spatial overlap was primarily checked by an optical microscope monitoring the sample surface, making use of the fact that the x-ray flux was high enough to excite luminescence from the platinum coating. The scattered light of the NIR laser, also visible on the microscope, was then simply directed to the position of this luminescence. Fine adjustment was achieved in an iterative way by monitoring the Hartmann-Shack sensor signal, centering precisely the laser spot on the heat bump. The time delay between x-ray and laser pulse was controlled electronically using a delay generator which shifted the phase of the laser oscillator feedback loop. Temporal overlap at the sample position was obtained monitoring the photodiode signals.

The wavefront distortion measurement was performed in two steps: first the test laser wavefront and intensity were measured at the sensor position without heat load on the sample (non-distorted test beam). Thereafter, a train of 120 x-ray pulses was directed onto the sample, and the delayed NIR pulse reflected from the heated zone of the surface was registered by the Hartmann-Shack sensor at one kilohertz repetition rate (distorted test beam). For each delay 64 camera frames of 25 ms each were recorded and averaged, optimized according to the wavefront stability of the fs laser system. Thus, each wavefront and beam profile reconstruction contains information from 1600 x-ray bursts. After this measurement of the distorted beam, another record of the non-distorted beam was taken to check the remaining wavefront, giving a measure for the confidence level. The procedure was repeated for each delay time.

3. Surface profile reconstruction from wavefront measurement

3.1 Reconstruction method

An absolute wavefront calibration is obtained from a plane wave reference, making use of a 50X expanded HeNe laser. The displacement of the foci produced by the microlens array (21 x19 spots) from their reference positions samples the wavefront gradient, from which the wavefront is computed by fitting a set of Zernike polynomials (up to 6th order in the radial coordinate) [15] in a least squares approach. The wavefront reconstruction is described in greater detail in [16] and the Hartmann-Shack sensor in [17].

The surface topology of the sample is computed from the measured wavefronts as follows. We define a mirror coordinate system Σ which is described by the coordinates (ξ, η, ζ), where $\zeta = 0$ is the mirror surface. Let the plane of incidence be given by the ξ and ζ directions and let α be the angle of incidence of the test laser beam. The wavefront sensor-coordinate system S is described by the coordinates (x,y,z), where the z-axis is the optical axis of the test laser beam after reflection and $z = 0$ defines the detector plane. S follows from Σ by a rotation around the

η-axis by α and a translation along ζ by the distance L. For the scalar complex amplitude of the laser beam after reflection from the sample surface, we assume

$$U(\xi,\eta,0) = U_t(\xi,\eta,0)T(\xi,\eta),\qquad(1)$$

where U_t is the complex amplitude of the incident probe laser beam and $T(\xi,\eta)$ the complex phase factor imposed by the sample surface. Since the surface height deviation is small compared to the wavelength and the divergence is too large, we assume that the local transfer function is given by

$$T(\xi,\eta) = \exp\left(-2ik\cos(\alpha)\,\delta h(\xi,\eta)\right)\qquad(2)$$

with the wave vector k of the probe laser beam and the local surface height deviation from the non-distorted surface $\delta h(\xi,\eta)$.

Employing Huygens-Fresnel principle [15] and neglecting the inclination factor, we write

$$U(x,y,0) = -\frac{i}{\lambda}\iint d\xi d\eta\, U(\xi,\eta,0)\frac{\exp(ikR)}{R}.\qquad(3)$$

The squared distance $R^2(\xi_0, x_0)$ for a given point $\xi_0 = (\xi_0,\eta_0,0)$ on the mirror surface (in Σ) and point $x_0 = (x_0,y_0,0)$ in the detector plane (in S) is

$$R^2 = (x_0 - \xi_0\cos\alpha)^2 + (y_0 - \eta_0)^2 + (L + \xi_0\sin\alpha)^2.\qquad(4)$$

The Fresnel number $a^2/(L\lambda)$ of the optical system is approximately 0.2, where $\lambda = 0.8$ µm, beam radius $a = 250$ µm and distance sensor-sample $L = 410$ mm [15]. Hence R is expanded up to second order in ξ/z and x/z in the exponential and we use $L \approx R$ in the denominator. This yields the Kirchhoff-Fresnel-like propagation operator F for paraxial, quasi-monochromatic coherent beams [15], adapted for tilt. The back propagation onto the surface is given by $\hat{U}(\xi,\eta,0) = F^{-1}(U(x,y,0))$ with the inverse operator

$$\hat{U}(\xi,\eta,0) = F^{-1}(U(x,y,0)) = \frac{i\cos\alpha}{\lambda L}e^{-ikL}\exp\left(-\frac{ik}{2L}\left(\xi^2\cos^2\alpha + \eta^2\right)\right) \times$$
$$\iint dxdy\, U(x,y,0)\exp\left(-\frac{ik}{2L}\left(x^2+y^2\right)\right)\exp\left(\frac{ik}{L}\left(x\xi\cos\alpha + y\eta\right)\right)\qquad(5)$$

where $\hat{U}$ is the complex amplitude less tilt terms.

The phase factor follows from the ratio of the distorted and the non-distorted complex amplitude in the sample plane,

$$T(\xi,\eta) = \frac{F^{-1}(U_{distorted}(x,y,0))}{F^{-1}(U_{non-distorted}(x,y,0))},\qquad(6)$$

where the amplitudes $F^{-1}(U_{distorted})$, $F^{-1}(U_{non-distorted})$ are non-zero.

The integral (5) was solved on a 1500 x 1500 square grid, representing the circular evaluation area (2.85 mm radius) of the Hartmann-Shack sensor, using a Fast Fourier Transform (FFT) algorithm. Only information from microlenses within this area is used. The intensity between the individual spots on the CCD was interpolated by bicubic splines and the remaining grid points which correspond to a position outside the evaluation area are set to zero. The lateral resolution is given by $L\lambda/(2a)$ which is sufficient to resolve the expected sample distortion.

3.2 Results

After spatial filtering, the probe laser's wavefront at the Hartmann-Shack sensor position showed a remaining wavefront root-mean-square (w_{rms}) of about 20 nm relative to the HeNe

reference. Figure 2a shows a shot-to-shot fluctuation of 3.6 nm of the wavefront peak-to-valley (w_{pv}). The difference between the wavefront of the distorted and non-distorted beam is shown in Figs. 2b and 2c for a delay of 82µs (at the end of the x-ray burst) and 122µs. The w_{pv} at the sensor position grows for each pulse in the x-ray burst up to approximately 24nm. The mean stability of the reference wavefront was determined as described in section 2.2 and we found 2.1nm w_{pv} with standard deviation 1.1nm.
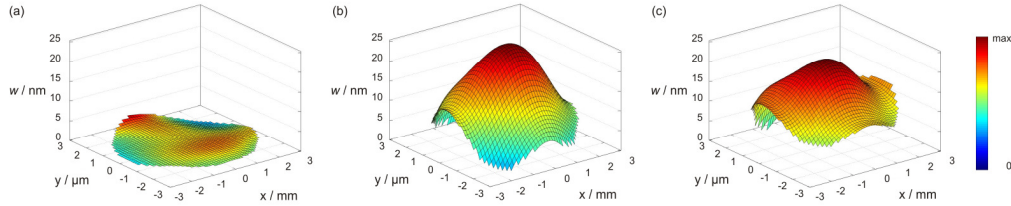

Fig. 2. (a) shows residual fluctuations in the wavefront of the test laser beam (3.6nm w_{pv}). The thermally induced wavefront distortion of the test laser at the sensor position is shown in (b) for a delay of 82µs (23.9nm w_{pv}) and in (c) for a delay of 122µs. (17.7nm w_{pv}).

The area extension of the wavefront distortion at the sensor position is wider than the x-ray spot size on the sample surface due to both diffraction and divergence of the probe laser beam. Thermal distortions for the delays 82 µs and 122 µs are plotted in Figs. 3a and 3b. The actual surface deformation (Figs. 3a, 3b) shows a near-Gaussian profile, which corresponds in size to the lateral dimensions of the x-ray spot and additionally a broader background.

The amplitude of the distortion is determined by fitting a Gaussian function of the form

$$h\left(\xi,\eta;h_0,h_1,\beta,\xi_0,\eta_0\right) = h_0 + h_1 \exp\left(-\frac{\xi'\left(\beta,\xi_0\right)^2}{2\sigma_\xi^2} - \frac{\eta'\left(\beta,\eta_0\right)^2}{2\sigma_\eta^2}\right), \tag{7}$$

where $\xi'(\beta,\xi_0)$ and $\eta'(\beta,\eta_0)$ are the the lateral coordinates on the sample surface which allow for decentring (ξ_0,η_0) and rotation (β) in the plane. Zero level is defined by the fit parameter h_0, since wavefront piston is generally not measurable using Hartmann-Shack sensors. A cross section along the η-axis is plotted in Fig. 3c for both the best-fit curve and the computed surface profile. The Gaussian fit yields a lateral surface distortion FWHM of 122 µm x 72 µm for 122 µs (Fig. 3) which corresponds to the x-ray beam diameter.
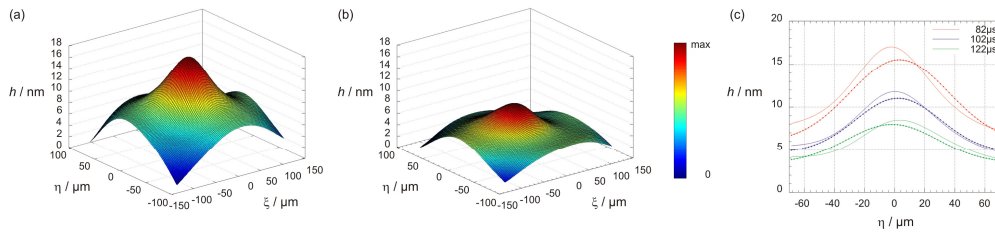

Fig. 3. (a) shows the reconstructed surface topology from wavefront measurements for a delay of 82µs (peak-to-valley (pv) 17nm) and (b) for a delay of 122µs (pv 8.6nm). The surface profiles correspond to the wavefronts shown in Figs. 2(b) and(c). Figure (c) shows a cross section of the surface profile along the η axis (solid lines) together with the three-dimensional Gaussian fit curve (dash-dotted).

Finally the bump height (fit parameter h_1) is plotted against the delay in Fig. 4. The maximum height bump is found to be 9.9 ± 0.2 nm. The experimental points can be exactly fitted using an exponential law. The decay has a time constant of 31 ± 6 µs, the error bar corresponding to the confidence interval of the fit.
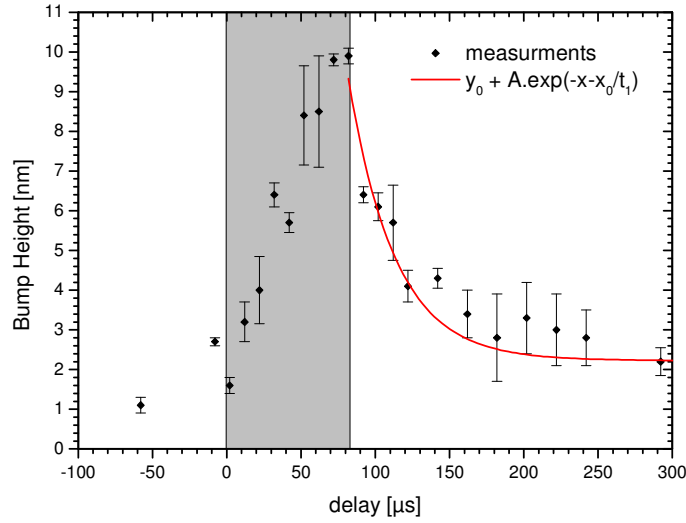
Fig. 4. Heat bump dynamics from wavefront measurement. The red line is the exponential decay used to fit the experimental points [t_1 = 31.1 µs].

4. Finite element method modeling

Finite elements simulations were performed to model the experimental conditions. Due to the symmetry of the beam shape only a quarter volume was modeled. The model then consists of a cylinder of 300 µm radius and 600 µm thick as shown in Fig. 5. The heat load was simulated using a 2 dimensional Gaussian distribution reproducing the x-ray beam profile. The profile along the propagation direction follows a regular exponential decay law. The absorbed power per unit of volume P can then be written as follows:

$$P(\mathrm{W}\cdot\mathrm{cm}^{-3}) = {p_0}\big/{V} \cdot \exp(-\frac{x^2}{2\sigma_x{}^2} - \frac{y^2}{2\sigma_y{}^2}) \cdot \exp(-\frac{z}{l_{\mathrm{abs}}}), \qquad (8)$$

where p_0 is the average power over a full bunch train equal to 3.72 W, $V = \pi\sigma_x\,\sigma_y\,l_{abs}$ is the volume where the absorption takes place, σ_x = 53.2 µm and σ_y = 27.2 µm are the rms value of the Gaussian profile calculated from the FWHM of the measured x-ray spot, and l_{abs} = 442 µm is the absorption depth at 15 keV in Si. The relevant thermo-dynamical constants used for the simulation are given in the Table 1. As the substrate is monocrystalline, with the surface being oriented along the (111) direction, the constants are then chosen accordingly to the relevant direction from Ref. [18]. These values were kept constant as the temperature variation is very weak, as shown in Fig. 5.

Table 1. Thermo-dynamical constants of Si (111) and Pt used in the FEM model

	Density	Poisson coefficient	Young modulus	Thermal expansion	Thermal conductivity	Specific heat
Material	g/cm3		GPa	10^{-6}/°C	W/m°C	J/g.°C
Si (111)	2.34	0.26	187	2.56 10^{-6}	163.3	0.703
Pt	21.4	0.36	275	9.0 10^{-6}	71.6	0.133

Figure 5 shows the simulated volume with color map showing the temperature at the end of the x-ray pulse train corresponding to the maximum bump. The maximum temperature rise is equal to 9.2 K leading to a maximum displacement is of 3.9 nm. Figure 6 shows the time

dependence of this displacement. The time constant for the decay can be also be retrieved assuming an exponential decay. The decay constant is then equal to 41.6 µs.
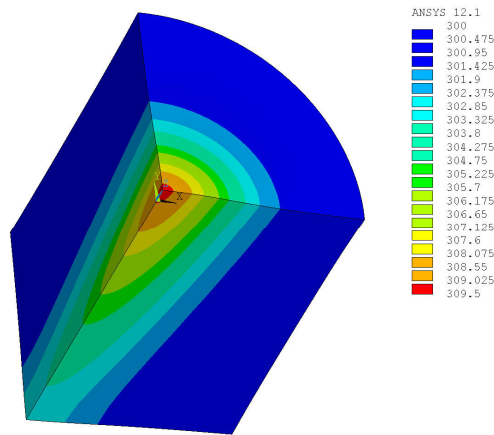

Fig. 5. Simulated volume with the FEM. The color shows the temperature in K at the end of the x-ray pulse train. The picture corresponds to the Si bare substrate.

In order to estimate the effect of the Pt coating, FEM simulations were also performed adding a 100 nm thick film on the top of the Si sample. We considered a constant load profile corresponding to 3% of absorption in the film and the same heat load profile in the Si substrate. Thin metallic coatings are usually polycrystalline, hence we used non direction-dependent thermo-dynamical constants as shown in Table 1. The results of the simulation are also shown in Fig. 6. The maximum bump height is found to be 4.2 nm with a maximum temperature rise of 11.3 K, decaying within 40.4 µs. As Pt has a larger thermal expansion, the height of the bump is a slightly larger. Nevertheless this clearly shows the very weak effect of the coating due to the low absorption of the thin layer.
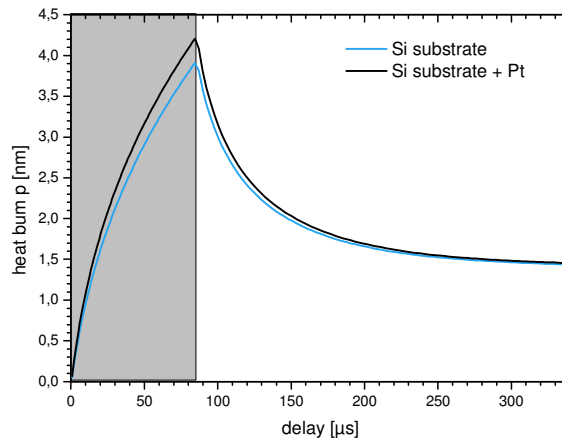

Fig. 6. Height of the surface point at the center of the simulated volume as a function of time resulting from FEM simulations. The blue curve is for the Si substrate and the black on for the Si + Pt coating.

Finally the temporal behavior can be understood by considering Fig. 5. It clearly shows that the heat gradient is much higher in the radial direction than along the depth. The heat flux is taking place primarily in the radial direction, which leads to the first fast decay of the heat

bump. On a longer time scale as the temperature gradient decreases, the heat flux also slows down inducing a long decay of the bump height. The simulation was run until a delay corresponding to 300 µs. Figure 6 clearly shows that at this delay the heat bump on the substrate has not yet completely disappeared.

5. Conclusion and discussion

The experiment and the FEM simulations give results in the same order of magnitude in terms of bump height (9.9 nm vs 4.2 nm,) and time constant (31.1µs vs 40.4 µs). Nevertheless there is a noticeable difference between the height of the bump experimentally measured and the one obtained with FEM simulations. This difference can be explained by the high repetition rate of the bunch train. As shown by the FEM results the bump firstly decreases rapidly within 30 to 40 µs and then relaxes slowly. Further FEM calculations indicate that after 1 ms the bump height is still in the range of 0.5 nm. As a result the pulse number n in the train, has a total height equal to $h = 4.2 + 0.5n$. As described in the section 2, the measurement procedure is done such that the wavefront is averaged over 25 ms, i.e. 26 bunch train at one kilohertz. The measured bump is then an average following the formula:

$$\frac{1}{26} * \sum_{n=0}^{25} 4.2 + 0.5 \cdot n = 10.45 \text{ nm}, \tag{9}$$

which is similar to the height of the bump we are measuring. Hence this clearly shows that the wide background, corresponding to the 0.5 nm, present in our measurement but difficult to be correctly subtracted is responsible for the discrepancy between model and experiment. On the other hand the agreement of the time constant is quite good and reflects the fact that the behavior of heat dissipation is primarily driven by the temperature gradient, i.e. the intensity profile of the beam.

   In this experiment we have measured the dynamics of a deformation in the nanometer range induced by a bunch train of x-ray pulses. We have shown that the deformation can be modeled with FEM simulations in a reasonable manner. Our results clearly show that nanometre scale deformation can be measured accurately which paves the way to practical applications and to further developments. As this technique is robust and easy to implement it can be used for in situ measurements providing real time measurements of the optics surface deformation. Moreover as underlined in Refs. [9,10], due to the high energy per pulse (in the mJ range) a single pulse of FEL can lead to the deformation of the optic relaxing on a nanosecond time scale. It is then questionable if in the case of high repetition rate facility the optical surface can be deformed from pulse to pulse. This fast process could then be studied with the technique we presented here, as the temporal resolution is limited only by the pump and probe pulse duration. Apart from the obvious technical interest, more fundamental questions on the behavior of materials under non equilibrium conditions would be addressed and answered.